Charge Transport and Antiferromagnetic Ordering in Nitroxide Radical Crystals

Journal:	*Molecular Systems Design & Engineering*
Manuscript ID	ME-ART-10-2022-000202.R1
Article Type:	Paper
Date Submitted by the Author:	14-Nov-2022

Complete List of Authors:	Liang, Zihao; Purdue University, Davidson School of Chemical Engineering Tan, Ying; Purdue University, Davidson School of Chemical Engineering Hsu, Sheng-Ning; Purdue University, Chemical Engineering; Purdue University Stoehr, Jacob; Purdue University, Davidson School of Chemical Engineering Tahir, Hamas; Purdue University, Davidson School of Chemical Engineering Woeppel, Aaron; Purdue University, Davidson School of Chemical Engineering Debnath, Suman; Purdue University, Davidson School of Chemical Engineering Zeller, Matthias; Youngstown State University, Department of Chemistry Dou, Letian; Purdue University, Chemical Engineering Savoie, Brett; Purdue University School of Chemical Engineering, Boudouris, Bryan; Purdue University, Davidson School of Chemical Engineering

Charge Transport and Antiferromagnetic Ordering in Nitroxide Radical Crystals

Zihao Liang,[†] Ying Tan,[†] Sheng-Ning Hsu,[†] Jacob F. Stoehr,[†] Hamas Tahir,[†] Aaron B. Woeppel,[†] Suman Debnath,[†] Matthias Zeller,[‡] Letian Dou,[†,§] Brett M. Savoie,[†] Bryan W. Boudouris[†,‡,]*

[†] Charles D. Davidson School of Chemical Engineering, Purdue University, 480 W Stadium Ave, West Lafayette, Indiana 47907, United States

[‡] Department of Chemistry, Purdue University, 560 Oval Drive, West Lafayette, Indiana 47907, United States

[§] Birck Nanotechnology Center, Purdue University, West Lafayette, Indiana 47907, United States

* To whom correspondence should be addressed: boudouris@purdue.edu

Design, System, Application (less than 200 words)

Chemistries that manipulate molecular packing in crystal structures were introduced into open-shell moieties to enhance spin-spin interactions in an intentional molecular design archetype. Although open-shell moieties have established electronic and magnetic properties, less attention has focused on using molecular engineering to enhance intermolecular interactions in these emerging molecular systems despite the promise that a combined computational-experimental approach could have in this established field. In this work, rigid biphenyl groups were introduced to nitroxide radical-bearing moieties to increase the tendency for the molecules to order in the solid state and crystallize. In fact, the introduction of this molecular design feature caused the radical groups to crystallize in a specific manner. In addition, alkyl chains were introduced to control the molecular packing in the crystal structures to achieve strong magnetic interactions between the open-shell moieties. Moreover, the close packing of the radical functionalities also generated a pathway to facilitate charge transport in a relatively facile manner. Therefore, these organic crystal materials can be applied into organic electronics due to their charge transport capabilities as well as spin labels due to their magnetic properties.

Charge Transport and Antiferromagnetic Ordering in Nitroxide Radical Crystals

Zihao Liang,[†] Ying Tan,[†] Sheng-Ning Hsu,[†] Jacob F. Stoehr,[†] Hamas Tahir,[†] Aaron B. Woeppel,[†] Suman Debnath,[†] Matthias Zeller,[‡] Letian Dou,[†,§] Brett M. Savoie,[†] Bryan W. Boudouris[†,‡,]*

[†] Charles D. Davidson School of Chemical Engineering, Purdue University, 480 W Stadium Ave, West Lafayette, Indiana 47907, United States

[‡] Department of Chemistry, Purdue University, 560 Oval Drive, West Lafayette, Indiana 47907, United States

[§] Birck Nanotechnology Center, Purdue University, West Lafayette, Indiana 47907, United States

* To whom correspondence should be addressed: boudouris@purdue.edu

Abstract. Nonconjugated radical polymers and small molecules are employed as functional materials in organic electronic devices. Furthermore, the unpaired electrons on these materials have permanent magnetic moments, making these materials promising candidates for organic magnets. Through molecular design, strong antiferromagnetic and ferromagnetic ordering has been achieved in conjugated materials. However, the magnetic properties of nonconjugated radical polymers have only shown weak magnetic interactions among the open-shell sites due to the large mean separation between radicals in typical materials. Here, we have designed, synthesized, and crystalized two open-shell molecules that used molecular engineering to control the assembly of the open-shell sites into a strong antiferromagnetically ordered network. The strong antiferromagnetic interaction is evidenced by a high paramagnetic-to-antiferromagnetic transition temperature of ~40 K. This high transition temperature was a result of a high spin exchange coupling constant J of about −20 cm^{-1}, which was suggested by both experimental and computed coupling parameters given by the energy difference between high-spin and low-spin broken-symmetry structures. In addition, a single-crystal electrical conductivity of ~10^{-3} S m^{-1} was achieved, which indicated the potential of this material in electronic applications. Therefore, this work provides an insight of a design strategy for radical-based electronic and magnetic materials through proper molecular structure modifications.

Introduction

Stable organic radicals have been used extensively in electronic,[1–9] electrochemical,[10–19] and magnetic field-responsive applications[20–29] because radical-based polymers and small molecules are proven electronic and ionic conductors.[30–35] Additionally, stable radical molecules have intriguing magnetic properties because the unpaired electrons of the radical sites interact with applied magnetic fields, and intermolecular spin-spin interactions inside these open-shell materials can result in ordered magnetic effects.[35–39] However, magnetism in organic radical materials is difficult to control because it depends on the interactions between the unpaired electrons, and therefore, the spatial arrangement of spins plays an important role in determining the overall magnetic behavior.[40,41]

Previously, noncovalent intermolecular interactions have been introduced to tune the magnetic properties of organic radical materials. More specifically, the influence of hydrogen bonding, π-π stacking, and London dispersion interactions on the magnetic interactions in solid crystals have been evaluated.[40] Additionally, the effect of the intramolecular configuration of the radical groups was established in nitroxide radical-based dendrimers.[42,43] However, the spin-spin interactions were not strong enough to overcome the thermal disturbance from the environment, and the magnetic orderings in nitroxide radical-based materials usually only exists at temperatures < 10 K. Therefore, an understanding of the relationship between structure and magnetic property needs to be established, and new molecular designs are needed to achieve stronger magnetic interactions in radical-based material systems.

Here, two nitroxide radical-based small molecules with n-alkyl groups were designed and synthesized, and their optical, electrochemical, and magnetic properties were quantified. Single crystals of both molecules were grown from solution. The two molecules are different in the length

of the alkyl substitution group. Specifically, one molecule had a hexyl chain, 4'-hexyl-[1,1'-biphenyl]-4-yl 1-hydroxyl-2,2,6,6-tetramethylpiperidine-4-carboxylate (C6BP-TEMPO), and the other molecule was substituted with a dodecyl chain, 4'-dodecyl-[1,1'-biphenyl]-4-yl 1-hydroxy-2,2,6,6-tetramethylpiperidine-4-carboxylate (C12BP-TEMPO). Despite the subtle differences at the atomic level, both molecules showed strong antiferromagnetic orderings in their crystals, and a relatively high Néel temperature of around 40 K was achieved, which is one of the highest transition temperatures for 2,2,6,6-tetramethylpiperidinyloxyl-bearing (TEMPO-bearing) open-shell materials reported to date. Using a longer alkyl chain in the molecule design, the radical moieties were forced to assemble closer in the crystal lattice, resulting in stronger spin-spin interactions. This was supported by the fact that strongly interacting radical dimers were present in C12BP-TEMPO crystals with a simulated spin exchange coupling constant $J = -31.1$ cm^{-1}. In comparison, the strongest radical dimer in C6BP-TEMPO only had $J = -26.9$ cm^{-1}. However, the long alkyl group impaired the overall spin-spin interactions on the macroscopic scale because the additional alkyl spacers weakened the interactions of the radical dimers in other configurations, as the overall J value for C12BP-TEMPO was about –21.0 cm^{-1}, which was weaker than C6BP-TEMPO (i.e., overall $J = -23.1$ cm^{-1}). In addition, this dilution effect from the increased carbon chain length resulted in an order of magnitude lower electrical conductivity in C12BP-TEMPO single crystals, as the single-crystal electrical conductivity at room temperature was ~6×10^{-4} and 1×10^{-5} S m^{-1} for C6BP-TEMPO and C12BP-TEMPO, respectively. These electrical conductivities increased with increasing temperatures in the range of 10 K ≤ T ≤ 300 K, and this dependency was fit into a variable-range hopping model. Therefore, this work highlights the impact of molecular engineering on the magnetic properties of radical molecules using a combined

computational and experimental approach, and the key results provide insights in designing future radical-based electronic and magnetic materials.

Results and Discussion

Two TEMPO radical-based molecules with n-alkyl substituted biphenyl cores were synthesized (i.e., C6BP-TEMPO and C12BP-TEMPO). These two molecules were targeted to quantify how the difference in the alkyl chain lengths altered the interlayer distance of the molecular packing inside the crystal structures. It was hypothesized that the long alkyl chain in C12BP-TEMPO would result in a looser packing of the molecules in the crystal lattice compared with C6BP-TEMPO. In turn, this change in crystal structure would impact the electrical and magnetic properties of the related materials. The intermediate products, 4'-hexyl-[1,1'-biphenyl]-4-ol (C6BPOH) and 4'-dodecyl-[1,1'-biphenyl]-4-ol (C12BPOH) were synthesized through a Suzuki coupling reaction between alkyl-substituted bromobenzene and 4-hydroxyphenylboronic acid pinacol ester (Scheme 1). Both molecules and their intermediate products were characterized by ^{1}H NMR spectroscopy, and the mass spectroscopy confirmed the successful synthesis of the two open-shell products (Figure S1-S6). The two radical molecules have been characterized by UPLC-MS, and the elution profiles show that no impurities appear in the products (Figure S7).

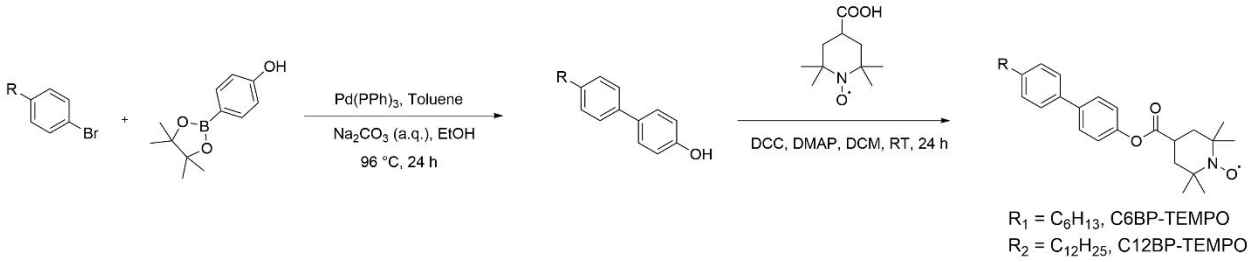

Scheme 1. Synthetic pathways of the n-alkyl substituted radical molecules. R is C_6H_{13} for C6BP-TEMPO and $C_{12}H_{25}$ for C12BP-TEMPO.

The successful introduction of the redox-active TEMPO radical moiety into the two biphenyl molecules was confirmed through multiple experimental techniques. First derivative

electron paramagnetic resonance (EPR) spectra of both molecules displayed a triplet pattern at a g-factor of 2.0089, which was a result of spin-nuclear coupling from the N-O bond on the TEMPO radical (Figure 1a). The spectra were integrated twice, then the integrated intensity was compared with that of the 4-hydroxy-TEMPO standard to give the radical content of C6BP-TEMPO and C12BP-TEMPO to be 96% and 99%, respectively. That is, no significant loss of open-shell moieties happened during the synthesis process.

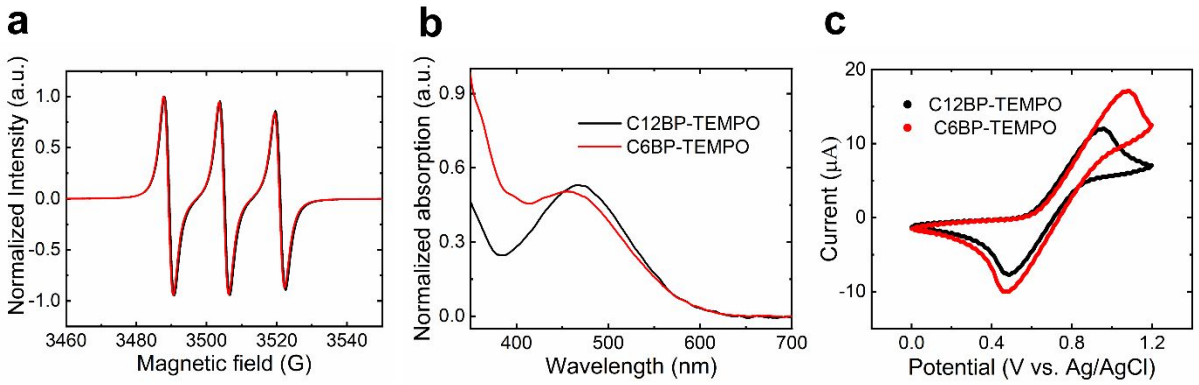

Figure 1. (a) Normalized 1st-derivative EPR spectra of C6BP-TEMPO and C12BP-TEMPO in chloroform with a concentration of 1 mg mL^{-1}. Here, the black and red lines refer to C6BP-TEMPO and C12BP-TEMPO, respectively. (b) Normalized UV-Vis light absorption spectra of the two TEMPO-based molecules in THF at a concentration of 1 mg mL^{-1}. (c) Cyclic voltammograms of C6BP-TEMPO and C12BP-TEMPO in their 30th cycle. Gold, platinum, and Ag/AgCl were used as working electrode, counter electrode, and reference electrode, respectively. The diagrams were recorded at a scan rate of 0.75 V s^{-1} in 0.1 M tetrabutylammonium hexafluorophosphate ($TBAPF_6$) in chloroform after 10 conditioning cycles.

Furthermore, the two molecules displayed similar ultraviolet-visible (UV-Vis) light absorption spectra with an absorption peak at around 456 nm, which is associated with the nitroxide radical moiety (Figure 1b). This is consistent with the absorption spectra from previous reports of nonconjugated radical polymers with nitroxide radical groups.[32] The reversible redox behavior of both molecules was confirmed by cyclic voltammetry (CV). Both molecules have robust redox stability and displayed similar redox voltammograms through 30 cycles, and the voltammogram of both molecules in their 30th cycle was shown in Figure 1c. The same reduction peak at +0.48 V

versus Ag/AgCl was observed for the two molecules, while the oxidation peak for C6BP-TEMPO showed up at a higher voltage than that of C12BP-TEMPO (i.e., +1.07 V and +0.95 V vs. Ag/AgCl for C6BP-TEMPO and C12BP-TEMPO, respectively). The oxidation and reduction behavior is associated with the TEMPO radical species on both molecules. The slightly lower oxidation potential observed for C12BP-TEMPO was an effect caused by the alkyl substitution group. The longer alkyl chain likely resulted in a thicker hydration shell, making anion uptake after oxidation easier, and this caused the oxidation to occur at a lower potential.

Single crystals of the two radical molecules were grown from solution by diffusing hexane vapor into their saturated ethyl acetate solutions. The macroscopic shapes of the single crystals for both molecules were flat plates. The crystal structures and phase purities of the single crystals were evaluated using X-ray diffraction (XRD) experiments. Because the two molecules are structurally similar, the single crystal structures for C6BP-TEMPO and C12BP-TEMPO are both triclinic. As shown in Figure S8, the crystal structure of C6BP-TEMPO belongs to the P-1 space group, and it has lattice parameters of: a = 5.60 Å, b = 8.08 Å, c = 27.30 Å and α = 83º, β = 88º, γ = 82º. The C12BP-TEMPO crystallized in the P-1 space group, and with lattice parameters of: a = 5.63 Å, b = 34.43 Å, c = 47.13 Å and α = 82º, β = 88º, γ = 86º. The melting temperature of C6BP-TEMPO and C12BP-TEMPO were 89 ℃ and 97 ℃, respectively, as shown in Figure S9.

A clear transition from paramagnetic to antiferromagnetic spin orderings in crystals of both radical molecules was revealed using superconducting quantum interference device (SQUID) magnetometer. In these experiments, single crystals were grown from solution, completely dried, and ground into smaller pieces for testing. When the temperature was decreased from 300 K, the molar magnetic susceptibility first increased because the molecules behave as a paramagnetic material when the temperature was above the Néel temperature (T_N). Decreasing the temperature

lowered the thermal energy of the system and suppressed spin flipping; this allowed the spins to align into the same direction. However, when the temperature was below T_N, the apparent magnetic susceptibility started to decrease instead of continuously following the paramagnetic behavior (Figure 2). This showed that antiferromagnetic ordering started to form below T_N. At around 10 K, the magnetic susceptibility sharply increased because of the paramagnetic impurities in the sample that are likely caused by the lattice defect in the crystals. Here, the paramagnetic impurities aligned into the same direction under the applied magnetic field to result in the sharp increase of the effective magnetic susceptibility.[37]

The paramagnetic behavior in the temperature range of 40 to 300 K can be described using the Curie-Weiss law. However, when the temperature is close to the magnetic transition at lower temperatures, deviations from the law can occur. Therefore, the inverse of molar magnetic susceptibility in the temperature range of 100 to 300 K was fit to the Curie-Weiss law (Equation 1), and the linearity of the data showed that paramagnetic behavior was dominant in that temperature range. This linearity has been observed in a previous report of a TEMPO-based paramagnetic radical polymer.[44]

$$\frac{1}{\chi_m} = \frac{T-\theta}{C} \qquad (1)$$

Here, C is the Curie constant and θ is the Weiss temperature. The Curie constants was about 0.629 and 0.307 emu K Oe^{-1} mol^{-1} for C6BP-TEMPO and C12BP-TEMPO, respectively. Then, the linear fitting was extrapolated to the cross-section with horizontal axis for both molecules, and the temperature at the crossing point revealed the Weiss temperature, which was about −82 K and −23 K for C6BP-TEMPO and C12BP-TEMPO, respectively. The fact that $\theta < 0$ is consistent with the idea that both molecules are antiferromagnetic materials.

The magnetic transition around T_N corresponds to a singlet-triplet transition, as the spins were aligned in pairs of opposite directions in antiferromagnetic behavior, while the spins were aligned into the same direction under the applied magnetic field in paramagnetic behavior.[27,40,41] Therefore, this transition can be approximately described using the Bleaney-Bowers equation (Equation 2) when S = 1/2.

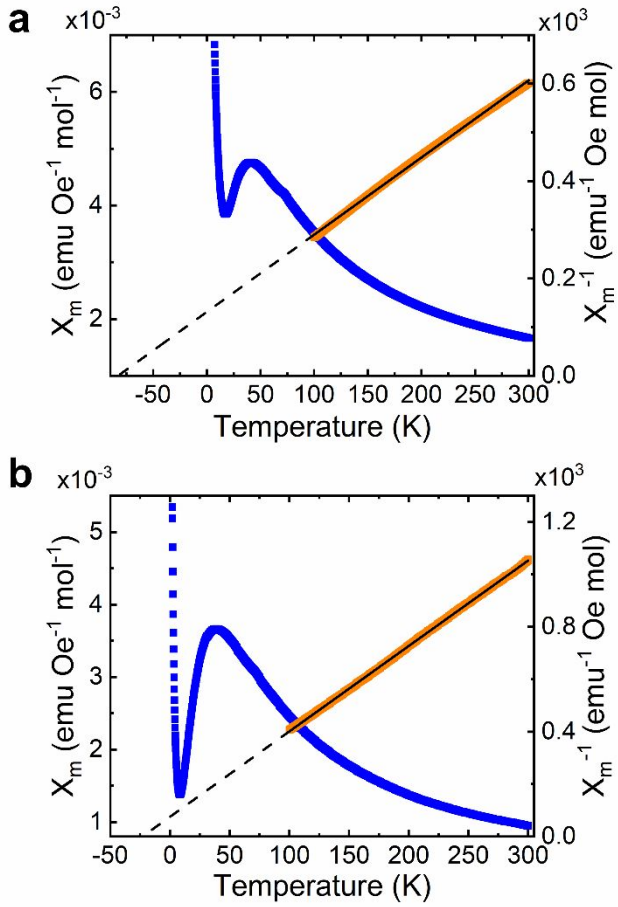

Figure 2. Molar magnetic susceptibility and its reciprocal for the (a) C6BP-TEMPO and (b) C12BP-TEMPO samples across a temperature range of 2 K to 300 K. The blue dots refer to the molar magnetic susceptibility (χ_m) and the orange dots are the reciprocal of χ_m. The black solid line shows the fits of χ_m^{-1} to the Curie-Weiss law in the range of 100 K < T < 300 K, and the dashed black line is the extrapolation of the fitting line, which reveals the Weiss temperature at the interception of the horizontal axis.

$$\chi_m = \frac{4C}{T \times (3 + e^{(-\frac{2J}{k_B T})})} \qquad (2)$$

Here, C is the Curie constant, J is the spin exchange coupling constant, and k_B is the Boltzmann constant.

The theoretical molar susceptibility at each temperature was calculated using the J value that resulted in a transition temperature closest to the experimental value. The theoretical curves were plotted along with the experimental curves in Figure 3. In this approximation process, the Curie constant was smaller than the theoretical value calculated from Curie-Weiss fitting. This deviation is because the diamagnetic portions (i.e., closed-shell portions in the molecular structure which has negative magnetic moments) in the sample have more contributions in the effective magnetic moments in the lower temperature region.[37] The spin-coupling constant (*J*) was approximated to be −23.2 cm^{-1} and −21 cm^{-1} for C6BP-TEMPO and C12BP-TEMPO, respectively. The negative *J* values indicate that the overall spin-spin interaction in the samples were antiferromagnetic.

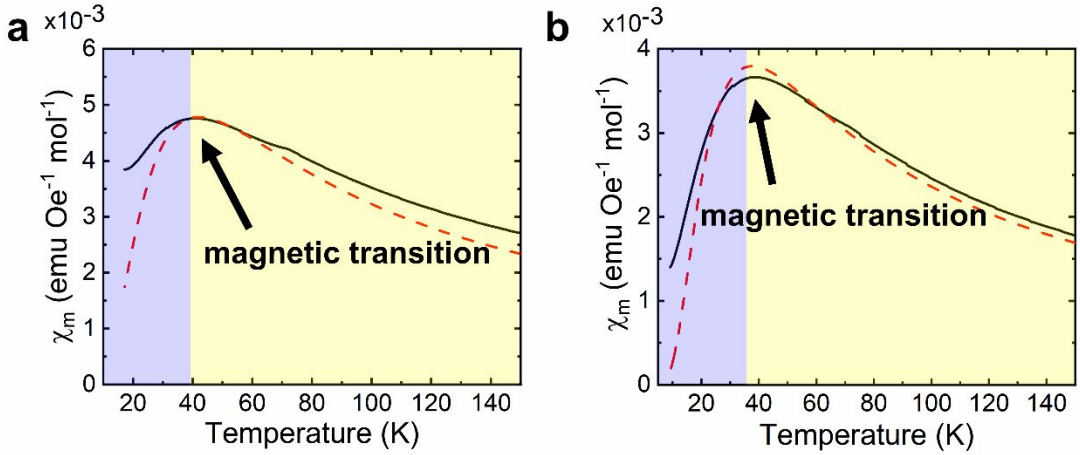

Figure 3. Molar magnetic susceptibility of (a) C6BP-TEMPO and (b) C12BP-TEMPO was fit to the Bleaney-Bowers equation for S = 1/2. Black curve is the experimental data, and red dashed curve is the calculated χ_m when (a) J = −23.2 cm^{-1}, C = 0.400 emu K Oe^{-1} mol^{-1} and (b) J = −21

cm^{-1}, C = 0.285 emu K Oe^{-1} mol^{-1}. The yellow region indicates the paramagnetic behavior, and the blue region indicates the antiferromagnetic behavior. The magnetic transition temperature (indicated by the arrow) of the calculated curve matches with the experimental curve.

On the other hand, the exchange coupling constants simulated from the energy difference between the high-spin and broken-symmetry solutions of the radical dimer system agreed well with the experimental observation. Because the major spin component was located on the nitroxide head, J-coupling calculations were performed for five TEMPO dimers taken from the crystal structure exhibiting the shortest nitroxyl oxygen-oxygen distances. The molecular design of alkyl chain drove the close contact between adjacent crystal layers, resulting in the closest nitroxide distances to be 3.51Å for C6BP-TEMPO and 3.48 Å for C12BP-TEMPO, with the high antiferromagnetic spin-coupling values (i.e., −26.93 cm^{-1} for C6BP-TEMPO and −31.13 cm^{-1} for C12BP-TEMPO). It should be noted that the spin coupling effects of other major dimer combinations found in the system are very weak. The nearest dimer configuration mainly contributed to the overall strong antiferromagnetic behaviors in agreement with the experimental extrapolations.

In addition to the unique antiferromagnetic behavior, both C6BP-TEMPO and C12BP-TEMPO single crystals transport charge. Here, the single-crystal electrical conductivities for both molecules have been quantified across a temperature range of $10 \leq T \leq 300$ K (Figure 5). In this temperature range, the conductivities for both molecules increased with increasing temperatures, and the dependance of electrical conductivity on temperature for both molecules was fit into a variable-range hopping (VRH) model (Equation 3), showing that both molecules transport charge under the same mechanism. During the varied temperature electrical testing, the thermal expansion of the metal electrodes caused changes in the contact resistance for the C6BP-TEMPO device, which caused deviation from model fitting above 100 K.

$$\sigma = \sigma_0 \, e^{-(T_0/T)^{1/(d+1)}} \qquad (3)$$

Here, T is the absolute temperature, and d, σ_0, and T_0 are constants. Because charge transport is 1-dimenstional in nature (i.e., along the long axis of the crystal), d was set as 1 in our analyses. The σ_0 and T_0 values were 3.7×10^{-3} S m^{-1} and 1037 K for C6BP-TEMPO, and 1.1×10^{-4} S m^{-1} and 1592 K for C12BP-TEMPO, respectively, as determined by the fit of the data to the VRH model.

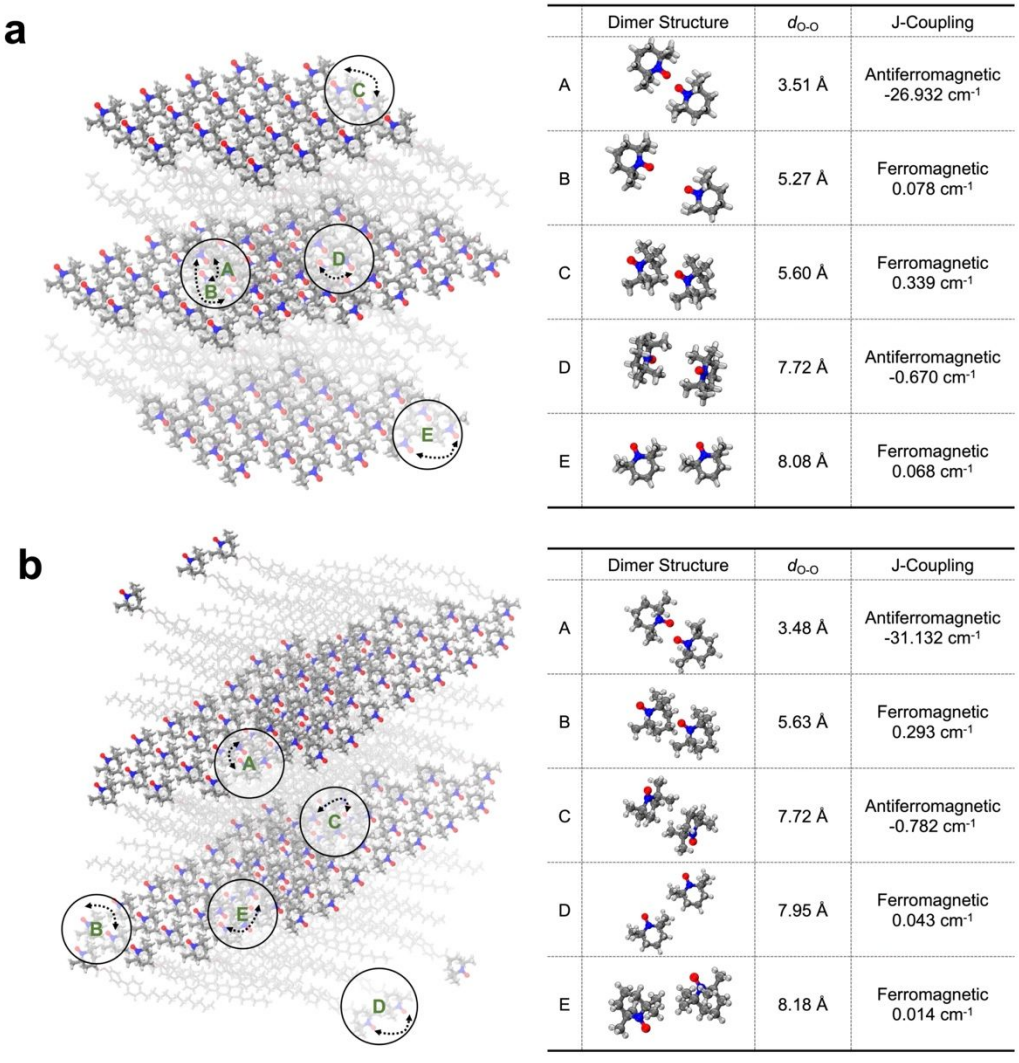

	Dimer Structure	$d_{O\text{-}O}$	J-Coupling
A		3.51 Å	Antiferromagnetic -26.932 cm^{-1}
B		5.27 Å	Ferromagnetic 0.078 cm^{-1}
C		5.60 Å	Ferromagnetic 0.339 cm^{-1}
D		7.72 Å	Antiferromagnetic -0.670 cm^{-1}
E		8.08 Å	Ferromagnetic 0.068 cm^{-1}

	Dimer Structure	$d_{O\text{-}O}$	J-Coupling
A		3.48 Å	Antiferromagnetic -31.132 cm^{-1}
B		5.63 Å	Ferromagnetic 0.293 cm^{-1}
C		7.72 Å	Antiferromagnetic -0.782 cm^{-1}
D		7.95 Å	Ferromagnetic 0.043 cm^{-1}
E		8.18 Å	Ferromagnetic 0.014 cm^{-1}

Figure 4. TEMPO alignments (highlighted regions) from crystallographic structures (shaded regions) and calculated J-Coupling values of five nearest nitroxyl dimers (circled in the structure on the left and values reported in the table on the right) of (a) C6BP-TEMPO and (b) C12BP-TEMPO. Atom representation: C – gray; O – red; N – blue; H – white.

The conductivities of C6BP-TEMPO and C12BP-TEMPO at room temperature were around 6×10^{-4} and 1×10^{-5} S m^{-1}, respectively. Three replicas of the devices for both molecules

were measured at room temperature, and the average conductivity and standard deviations were show in Figure S10. The conductivity values of C6BP-TEMPO were almost an order of magnitude higher than that of C12BP-TEMPO at the same temperature. This was potentially because the longer alkyl chains caused looser molecular packing in the overall crystal structures, which was indicated by two facts. These are that: (1) the average volume occupied for each molecule in its unit cell for C6BP-TEMPO and C12BP-TEMPO was 606 and 753 $Å^3$ and (2) the interlayer distances of the TEMPO functionalities are 27.30 and 34.43 Å for C6BP-TEMPO and C12BP-TEMPO, respectively. In the same way, the electrical communication between the open-shell moieties in C12BP-TEMPO was weaker because electrons need to hop across a larger distance in average to achieve charge transportation.

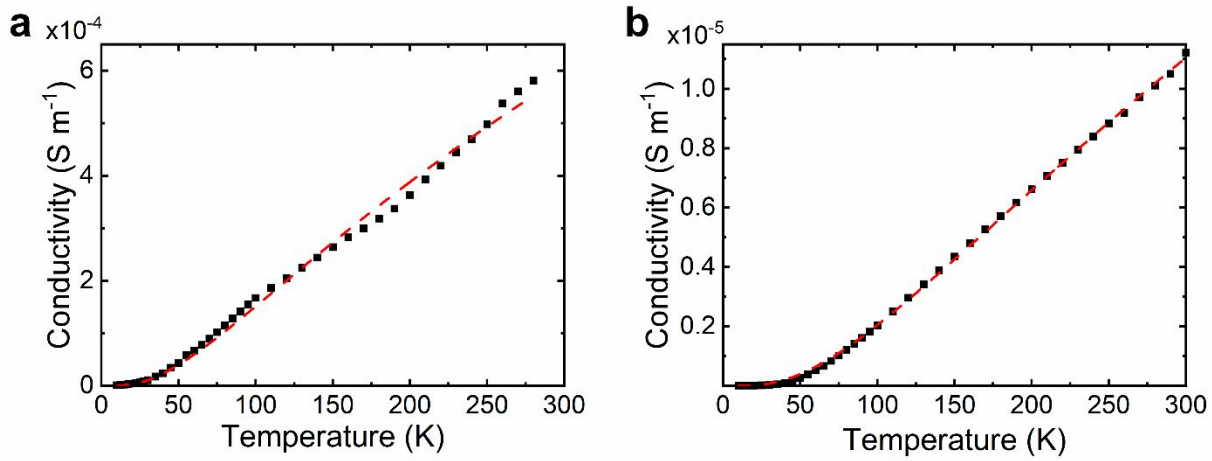

Figure 5. Electrical conductivities of (a) C6BP-TEMPO and (b) C12BP-TEMPO single crystals across a temperature range of $10 \leq T \leq 300$ K as measured. The conductivity of single crystals of both molecules increased as temperature increased, and the dependance of conductivity on temperature can be fit into a variable-range hopping model for both molecules. The conductivity of C6BP-TEMPO is one order of magnetite higher than that of C12BP-TEMPO at the same temperature.

Conclusion

By introducing alkyl functionalities on the molecular structures of TEMPO-bearing molecular systems, strong antiferromagnetic orderings are achieved in organic radical crystals with

a relatively high Néel temperature of around 40 K. Such a high transition temperature was the result of the high overall spin-exchange coupling constants of about –20 cm^{-1}. Computed spin coupling parameters suggested the strong magnetic interactions between the radical sites in the crystals. Although the longer alkyl chain of C12BP-TEMPO resulted in closer distances between the adjacent radical layer, which generated strongly interacting radical dimers with a simulated spin exchange coupling constant $J = -31.1$ cm^{-1}, the overall magnetic coupling was impaired by the excess of alkyl chain length. This dilution effect had huge impact on the electronic properties, as the single-crystal electrical conductivity of C12BP-TEMPO was one order of magnetite lower than that of C6BP-TEMPO, with their conductivities at room temperature determined to be $\sim 6 \times 10^{-4}$ and 1×10^{-5} S m^{-1} for C6BP-TEMPO and C12BP-TEMPO, respectively. The electrical conductivities increased with increasing temperatures in the range of $10\ K \leq T \leq 300\ K$. In summary, introducing alkyl functional groups can manipulate the charge transport and magnetic orderings in nitroxide radical-based organic crystals, but the length of the alkyl chain needs to be controlled. These key results provide an insight of how to design radical-based electronic and magnetic materials through proper molecular structure modifications.

Experimental

Materials and general methods

All reagents were purchased from Sigma-Aldrich unless otherwise specified. Also, 4-Carboxy-2,2,6,6-tetramethylpiperidinl-oxyl (97%) were purchased from TCI America. All reagents were used as they were received without further purification except that toluene was passed through a Puresolv solvent purification system before use. Silicon dioxide substrates used in the electrical characterization were purchased from Silicon Valley Microelectronics, Inc.

General methods

Electron paramagnetic resonance (EPR) spectroscopy data were collected using a Bruker EPR-EMX spectrometer. In these experiments, C6BP-TEMPO and C12BP-TEMPO were dissolved in anhydrous chloroform at a concentration of 1 mg mL^{-1}, and the 4-hydroxy-TEMPO standard was prepared in the same way. Ultraviolet-visible (UV-Vis) light spectroscopy data were collected within the wavelength range of $350 \leq \lambda \leq 700$ nm using a Cary 60 spectrometer. Mass spectra were obtained using a Thermo Finnigan LTQ orbitrap mass spectrometer with an electrospray ionization (ESI) probe, and positively charged ions were detected in the ESI mode. The ^{1}H nuclear magnetic resonance (NMR) spectra were collected using a Bruker AV-III-400-HD NMR spectrometer using solutions of ~1% (by weight) materials in deuterated dimethyl sulfoxide (d_6-DMSO) or deuterated chloroform ($CDCl_3$). In these experiments, the radical sites on the C6BP-TEMPO and C12BP-TEMPO molecules were quenched using L-ascorbic acid. Differential scanning calorimetry (DSC) data were collected using a TA Instruments Q20 Series calorimeter. In these experiments, around 2 mg of the single crystal samples were sealed in Tzero hermetic pans and initially heated to 110 ℃, held isothermally for 5 min, then cooled to 0 ℃ under a nitrogen purge. Then, these samples were heated and cooled again in the same temperature range, and the data were collected from the 2nd

heating and cooling cycle. All the ultra-performance liquid chromatography-mass spectrometry (UPLC-MS) experiments were performed on a Waters H-Class UPLC system with a SQD2 single quadrupole mass spectrometer, which is equipped with an electrospray ionization (ESI) source. The concentration of all the sample was 0.02 mg mL^{-1} in acetonitrile. Samples were injected into a flow of mobile phase with the mixture of water and acetonitrile. The separation was on a UPLC BEH C18 (nonpolar) column (130 Å, 1.7 micrometer, 2.1 mm × 50 mm) as a stationary phase.

Synthesis of 4'-hexyl-[1,1'-biphenyl]-4-ol (C6BPOH)

In a 20 mL Schlenk tube, 4-hydroxyphenylboronic acid pinacol ester (220 mg, 1 mmol) sodium carbonate (212 mg, 2 mmol), and tetrakis(triphenylphosphine)palladium(0) (56 mg, 0.05 mmol) were dissolved in 0.5 mL of ethanol and 0.5 mL of deionized water. Then, 1-bromo-4-*N*-hexylbenzene (288 mg, 1.2 mmol) dissolved in 1 mL of toluene was added, and the reaction vessel was degassed of oxygen on a Schlenk line with three freeze-pump-thaw cycles. This reaction mixture was stirred for 24 h at 96 °C. Once the reaction concluded, the precipitate generated was removed by filtration, washed with dichloromethane for three times, and the clear solution was collected and concentrated using a rotary evaporator. The reaction mixture was purified by column chromatography on silica gel with hexane: ethyl acetate 8:1 v/v serving as the eluent to recover 127 mg of the product as a light-yellow solid (yield = 50%). ^{1}H NMR (400 MHz, DMSO) δ 9.45 (s, 1H), 7.48 – 7.38 (m, 4H), 7.23 – 7.16 (m, 2H), 6.84 – 6.76 (m, 2H), 2.60 – 2.51 (m, 2H), 1.55 (t, J = 7.4 Hz, 2H), 1.32 – 1.19 (m, 6H), 0.88 – 0.80 (m, 3H).

Synthesis of 4'-dodecyl-[1,1'-biphenyl]-4-ol (C12BPOH)

In a 20 mL Schlenk tube, 4-hydroxyphenylboronic acid pinacol ester (220 mg, 1.1 mmol), sodium carbonate (212 mg, 2 mmol), and tetrakis(triphenylphosphine)palladium(0) (56 mg, 0.05 mmol) were dissolved in 0.5 mL of ethanol and 0.5 mL of water. Then, 1-bromo-4-*N*-dodecylbenzene

(390 mg, 1.2 mmol) was dissolved in 1 mL of toluene was added, and the reaction vessel was degassed of oxygen on a Schlenk line with three freeze-pump-thaw cycles. This reaction mixture was stirred for 24 h at 96 °C under reduced pressure. Once the reaction concluded, the precipitate generated was removed by vacuum filtration, and the clear solution was collected and concentrated using a rotary evaporator. The mixture was purified by column chromatography on silica gel with hexane: ethyl acetate 8:1 v/v serving as the eluent to recover 120 mg of the product as a light-yellow solid (yield = 37%). ^{1}H NMR (400 MHz, DMSO) δ 9.45 (s, 1H), 7.48 – 7.38 (m, 4H), 7.22 – 7.15 (m, 2H), 6.84 – 6.76 (m, 2H), 2.59 – 2.51 (m, 2H), 1.55 (t, J = 7.4 Hz, 2H), 1.21 (s, 18H), 0.87 – 0.79 (m, 3H).

Synthesis of 4'-hexyl-[1,1'-biphenyl]-4-yl 1-hydroxyl-2,2,6,6-tetramethylpiperidine-4-carboxylate (C6BP-TEMPO)

In a 100 mL round bottom flask, 4-carboxy-2,2,6,6-tetramethylpiperidin1-oxyl (132 mg, 0.66 mmol) and N,N'-dicyclohexylcarbodiimide (DCC) (154 mg, 0.75 mmol) were dissolved in 5 mL of anhydrous dichloromethane (DCM). This mixture was stirred for 30 min, and a white precipitate was generated. Then, C6BPOH (127 mg, 0.5 mmol) and 4-dimethylaminopyridine (DMAP) (6 mg, 0.05 mmol) were added to the mixture and was stirred for 24 h at room temperature. Once the reaction concluded, the precipitate generated was removed by vacuum filtration, and the clear solution was collected and concentrated using a rotary evaporator. The mixture was purified by column chromatography on silica gel with hexane: ethyl acetate = 8:1 v/v serving as the eluent to recover 163 mg of the product as orange solid (yield = 75%) ^{1}H NMR (400 MHz, $CDCl_3$) δ 7.66 – 7.56 (m, 2H), 7.50 (d, J = 8.0 Hz, 2H), 7.27 (d, J = 9.2 Hz, 2H), 7.15 (d, J = 8.5 Hz, 2H), 2.97 (t, J = 12.6 Hz, 1H), 2.67 (t, J = 7.7 Hz, 2H), 2.02 (d, J = 15.0 Hz, 2H), 1.83 (t, J = 13.0 Hz, 2H), 1.67 (t, J = 7.2 Hz, 2H), 1.35 (s, 4H), 1.26 (d, J = 16.5 Hz, 12H), 0.91 (d, J = 4.6 Hz, 3H).

Synthesis of 4'-dodecyl-[1,1'-biphenyl]-4-yl 1-hydroxyl-2,2,6,6-tetramethylpiperidine-4-carboxylate (C12BP-TEMPO)

In a 100 mL round bottom flask, 4-carboxy-2,2,6,6-tetramethylpiperidin1-oxyl (94 mg, 0.43 mmol) and DCC (109 mg, 0.53 mmol) were dissolved in 5 mL of anhydrous dichloromethane (DCM). The mixture was stirred for 30 min, and a white precipitate was generated. Then, C12BPOH (120 mg, 0.36 mmol) and DMAP (4.3 mg, 0.04 mmol) were added, and the reaction mixture was stirred for 24 h at room temperature. Once the reaction concluded, the precipitate generated was removed by vacuum filtration, and the clear solution was collected and concentrated using a rotary evaporator. The mixture was purified by column chromatography on silica gel with hexane: ethyl acetate = 8:1 v/v serving as the eluent to recover 152 mg of the product as orange solid (yield = 81%) ^{1}H NMR (400 MHz, $CDCl_3$) δ 7.58 (d, J = 8.6 Hz, 2H), 7.49 (d, J = 8.2 Hz, 2H), 7.26 (d, J = 3.1 Hz, 2H), 7.13 (d, J = 8.6 Hz, 2H), 2.96 (tt, J = 12.7, 3.4 Hz, 1H), 2.65 (t, J = 7.7 Hz, 2H), 2.04 – 1.98 (m, 2H), 1.83 (t, J = 12.9 Hz, 2H), 1.68 – 1.64 (m, 2H), 1.29 – 1.23 (m, 30H), 0.90 (d, J = 6.4 Hz, 3H).

Single crystal growth and characterization

Single crystals of C6BP-TEMPO and C12BP-TEMPO were grown from solution using the anti-solvent vapor diffusion method. For both molecules, saturated solutions in ethyl acetate were loaded into a glass tube with a diameter of 5 mm. Then, this glass tube was placed in a glass tube with a diameter of 100 mm that was loaded with hexanes. This setup was capped tightly using a rubber septum and placed in a cabinet with no disturbance for 10 days. Plates of the single crystals with a light-orange color were obtained on the walls of the inner tube. Single crystals were quickly transferred to the goniometer head of a Bruker Quest diffractometer with a κ-geometry, an I-μ-S microsource X-ray tube, laterally graded multilayer (Goebel) mirror single crystal for

monochromatization, a Photon-III C14 area detector and an Oxford Cryosystems low temperature device. Examination and data collection were performed with Cu K_α radiation (λ = 1.54178 Å) or Mo K_α radiation (λ = 0.71073 Å) at 150 K. Additional data collection and refinement details can be found in the Electronic Supplementary Information (ESI).

Electronic conductivity measurements

The single crystals were removed from glass tubes and transferred on a silicon substrate with a 300 nm-thick oxide layer using a syringe needle. Then, the crystals were cleaned by drops of ethyl acetate and spin-dried at 1,000 rpm for 30 s on a spin coater. Then, 100 nm of gold and 400 nm of silver were deposited as electrodes by thermal evaporation using a silver wire (radius ~ 140 μm) as the shadow mask. The electrical conductivity measurements of the single crystals were performed under vacuum inside a LakeShore CRX-VF probe station using a Keithley 2450 source meter. The measurements were performed across a temperature range of 10 K ≤ T ≤ 300 K. with a step size of 10 K. Each temperature was held for 15 min prior to any current-voltage scan to ensure the temperature stability during the data collecting.

SQUID magnetometry

The magnetic susceptibility of the two molecules were measured at a temperature range of 2 K to 300 K. In the measurement of both molecules, single crystals were first grown from solution, and solvents were fully removed by slow drying in the cabinet. Then, about 3 mg of the single crystals were ground into small pieces with plastic spatula before being loaded into the polycarbonate sample testing capsules. The measurements were performed using the vibrating sample mode under a small magnetic field of 1000 Oe. The magnetic susceptibility was corrected for the contribution of the sample holder, and the contribution from the diamagnetic closed-shell

portions in the molecules was also corrected using Pascal's constants (-3.04×10^{-4} and -3.77×10^{-4} emu mol^{-1} for C6BP-TEMPO and C12BP-TEMPO, respectively).

Computational Details

The individual TEMPO radical geometries were stripped from crystallographic structures of C6BP-TEMPO and C12BP-TEMPO provided by XRD. The five dimer structures with the closest nitroxyl oxygen−oxygen distances were utilized for further analysis and reported in the main text. For each radical dimer set, both high-spin (HS) (approximate triplet) and broken-symmetry (BS) configurations were obtained from a self-consistent field (SCF) procedure with the ωB97X-D3 functional and the def2-TZVP basis set as implemented in Orca v4.1.2.[45] Their magnetic exchange couplings (J_{AB}) were computed from the energy difference between the HS and BS spin systems, as shown in the following formalism (Equation 4), which is approximately valid over the whole (weak/strong) coupling strength regime.[46]

$$J_{AB} = -\frac{(E_{HS} - E_{BS})}{\langle S^2 \rangle_{HS} - \langle S^2 \rangle_{BS}} \quad (4)$$

Here, $\langle S^2 \rangle_{HS}$ and $\langle S^2 \rangle_{BS}$ are the expected values for the square of the total spin operator, E_{HS} and E_{BS} are the single point energy of the high-spin and broken-symmetry state.

Acknowledgements

This work was supported by the U.S. Department of Energy, Office of Science, Basic Energy Sciences under Award DE-SC0021967 (Program Manager: Dr. Craig Henderson). We thank the Department of Energy for this generous support. The work on the single-crystal X-ray diffractions was supported by the National Science Foundation through the Major Research Instrumentation Program under Award CHE 1625543. The work on mass spectroscopy was supported in part by the Research Instrumentation Center in the Department of Chemistry at Purdue University.

References

1 L. Ji, J. Shi, J. Wei, T. Yu and W. Huang, *Advanced Materials*, 2020, **32**, 1–15.

2 Y. Tan, S. N. Hsu, H. Tahir, L. Dou, B. M. Savoie and B. W. Boudouris, *J Am Chem Soc*, 2022, **144**, 626–647.

3 Z. X. Chen, Y. Li and F. Huang, *Chem*, 2021, **7**, 288–332.

4 T. Chi, S. Akkiraju, Z. Liang, Y. Tan, H. J. Kim, X. Zhao, B. M. Savoie and B. W. Boudouris, *Polymer Chemistry*, 2021, **12**, 1448–1457.

5 L. Rostro, L. Galicia and B. W. Boudouris, *Journal of Polymer Science, Part B: Polymer Physics*, 2015, **53**, 311–316.

6 L. Zheng, S. Mukherjee, K. Wang, M. E. Hay, B. W. Boudouris and X. Gong, *Journal of Materials Chemistry A*, 2017, **5**, 23831–23839.

7 Y. Joo, L. Huang, N. Eedugurala, A. E. London, A. Kumar, B. M. Wong, B. W. Boudouris and J. D. Azoulay, *Macromolecules*, 2018, **51**, 3886–3894.

8 E. P. Tomlinson, M. J. Willmore, X. Zhu, S. W. A. Hilsmier and B. W. Boudouris, *ACS Applied Materials and Interfaces*, 2015, **7**, 18195–18200.

9 S. H. Sung, N. Bajaj, J. F. Rhoads, G. T. Chiu and B. W. Boudouris, *Organic Electronics*, 2016, **37**, 148–154.

10 H. J. Kim, K. Perera, Z. Liang, B. Bowen, J. Mei and B. W. Boudouris, *ACS Macro Letters*, 2022, **11**, 243–250.

11 J. T. Price, J. A. Paquette, C. S. Harrison, R. Bauld, G. Fanchini and J. B. Gilroy, *Polymer Chemistry*, 2014, **5**, 5223–5226.

12 S. Wang, A. D. Easley and J. L. Lutkenhaus, *ACS Macro Letters*, 2020, **9**, 358–370.

13 S. Akkiraju, J. Vergados, L. Hoagland, Z. Lu, V. Anandan and B. W. Boudouris, *Macromolecules*, 2021, **54**, 5178–5186.

14 T. Jähnert, B. Häupler, T. Janoschka, M. D. Hager and U. S. Schubert, *Macromolecular Rapid Communications*, 2014, **35**, 882–887.

15 T. Suga, Y. J. Pu, S. Kasatori and H. Nishide, *Macromolecules*, 2007, **40**, 3167–3173.

16 K. Oyaizu, T. Kawamoto, T. Suga and H. Nishide, *Macromolecules*, 2010, **43**, 10382–10389.

17 K. Oyaizu and H. Nishide, *Advanced Materials*, 2009, **21**, 2339–2344.

18 K. Zhang, M. J. Monteiro and Z. Jia, *Polymer Chemistry*, 2016, **7**, 5589–5614.

19 J. Chung, A. Khot, B. M. Savoie and B. W. Boudouris, *ACS Macro Letters*, 2020, **9**, 646–655.

20 B. Bleaney and K. D. Bowers, *Proceedings of the Royal Society of London. Series A. Mathematical and Physical Sciences*, 1994, **416**, 197–207.

21 G. Huang, C. Daiguebonne, G. Calvez, Y. Suffren, O. Guillou, T. Guizouarn, B. le Guennic, O. Cador and K. Bernot, *Inorganic Chemistry*, 2018, **57**, 11044–11057.

22 Y. L. Gao, S. Nishihara and K. Inoue, *CrystEngComm*, 2018, **20**, 2961–2967.

23 H. Jobelius, N. Wagner, G. Schnakenburg and A. Meyer, *Molecules*, 2018, **23**, 1–24.

24 K. Awaga and Y. Maruyama, *The Journal of Chemical Physics*, 1989, **91**, 2743–2747.

25 A. Rajca, *Chemistry - A European Journal*, 2002, **8**, 4834–4841.

26 H. Nishide, T. Maeda, K. Oyaizu and E. Tsuchida, *Journal of Organic Chemistry*, 1999, **64**, 7129–7134.

27 D. J. Adams, K. S. Mayer, M. Steelman and J. D. Azoulay, *The Journal of Physical Chemistry C*, 2022, **126**, 5701-5710.

28 S. Kumar, Y. Kumar, S. K. Keshri and P. Mukhopadhyay, *Magnetochemistry*, 2016, **2**, 42.

29 H. Nishide, T. Kaneko, T. Nii, K. Katoh, E. Tsuchida and P. M. Lahti, *J Am Chem Soc*, 1996, **118**, 9695–9704.

30 Y. Tan, N. C. Casetti, B. W. Boudouris and B. M. Savoie, *J Am Chem Soc*, 2021, **143**, 11994–12002.

31 S. Mukherjee and B.W. Boudouris, *Organic Raical Polymers: New Avenues in Organic Electronics*, Springer, Berlin, Germany, 2017.

32 L. Rostro, A. G. Baradwaj and B. W. Boudouris, *ACS Applied Materials and Interfaces*, 2013, **5**, 9896–9901.

33 L. Rostro, S. H. Wong and B. W. Boudouris, *Macromolecules*, 2014, **47**, 3713–3719.

34 Y. Joo, V. Agarkar, S. H. Sung, B. M. Savoie and B. W. Boudouris, *Science*, 2018, **359**, 1391–1395.

35 S. Fukami, V. O. Lorenz and O. Gomonay, *Journal of Applied Physics*, 2020, **128**, 3–6.

36 S. Aboaku, A. Paduan-Filho, V. Bindilatti, N. F. Oliveira, J. A. Schlueter and P. M. Lahti, *Chemistry of Materials*, 2011, **23**, 4844–4856.

37 S. Aonuma, H. Casellas, C. Faulmann, B. G. de Bonneval, I. Malfant, P. Cassoux, P. G. Lacroix, Y. Hosokoshi and K. Inoue, *Journal of Materials Chemistry*, 2001, **11**, 337–345.

38 T. Nogami and T. Ishida, *Molecular Crystals and Liquid Crystals Science and Technology Section A: Molecular Crystals and Liquid Crystals*, 1997, **296**, 305–322.

39 L. Zhu, K. L. Yao and Z. L. Liu, *Journal of Magnetism and Magnetic Materials*, 2006, **301**, 301–307.

40 J. Exner, S. Eusterwiemann, O. Janka, C. Doerenkamp, A. Massolle, O. Niehaus, C. G. Daniliuc, R. Pöttgen, J. Neugebauer, A. Studer and H. Eckert, *Physical Chemistry Chemical Physics*, 2018, **20**, 28979–28983.

41 O. Kahn, *Molecular Magnetism*, VCH Publishers, Inc., New York City, USA, 1993.

42 H. Yeo, S. Akkiraju, Y. Tan, H. Tahir, N. R. Dilley, B. M. Savoie and B. W. Boudouris, *ACS Polymers Au*, 2022, **2**, 59–68.

43 M. Gurská, V. Brezová, I. Šalitroš, Ľ. Švorc, I. Špánik, J. Moncoľ, J. Pavlik and P. Szolcsányi, *Chempluschem*, 2021, **86**, 396–405.

44 K. Zhang, Y. Hu, L. Wang, J. Fan, M. J. Monteiro and Z. Jia, *Polym. Chem.*, 2017, **8**, 1815–1823.

45 F. Neese, *Wiley Interdisciplinary Reviews: Computational Molecular Science*, 2012, **2**, 73–78.

46 T. Soda, Y. Kitagawa, T. Onishi, Y. Takano, Y. Shigeta, H. Nagao, Y. Yoshioka and K. Yamaguchi, *Chemical Physics Letters*, 2000, **319**, 223–230.